

A Deep *Chandra* ACIS Study of NGC 4151. II. The Innermost Emission Line Region and Strong Evidence for Radio Jet–NLR Cloud Collision

Junfeng Wang¹, Giuseppina Fabbiano¹, Martin Elvis¹, Guido Risaliti^{1,2}, Carole G. Mundell³, Margarita Karovska¹ and Andreas Zezas^{1,4}

juwang@cfa.harvard.edu

ABSTRACT

We have studied the X-ray emission within the inner ~ 150 pc radius of NGC 4151 by constructing high spatial resolution emission line images of blended OVII, OVIII, and NeIX. These maps show extended structures that are spatially correlated with the radio outflow and optical [OIII] emission. We find strong evidence for jet–gas cloud interaction, including morphological correspondences with regions of X-ray enhancement, peaks of near-infrared [FeII] emission, and optical clouds. In these regions, moreover, we find evidence of elevated NeIX/OVII ratios; the X-ray emission of these regions also exceeds that expected from nuclear photoionization. Spectral fitting reveals the presence of a collisionally ionized component. The thermal energy of the hot gas suggests that $\gtrsim 0.1\%$ of the estimated jet power is deposited into the host interstellar medium through interaction between the radio jet and the dense medium of the circum-nuclear region. We find possible pressure equilibrium between the collisionally ionized hot gas and the photoionized line-emitting cool clouds. We also obtain constraints on the extended iron and silicon fluorescent emission. Both lines are spatially unresolved. The upper limit on the contribution of an extended emission region to the Fe K α emission is $\lesssim 5\%$ of the total, in disagreement with a previous claim that 65% of the Fe K α emission originates in the extended narrow line region.

¹Harvard-Smithsonian Center for Astrophysics, 60 Garden St, Cambridge, MA 02138

²INAF-Arcetri Observatory, Largo E, Fermi 5, I-50125 Firenze, Italy

³Astrophysics Research Institute, Liverpool John Moores University, Birkenhead CH41 1LD, UK

⁴Physics Department, University of Crete, P.O. Box 2208, GR-710 03, Heraklion, Crete, Greece

Subject headings: X-rays: galaxies — galaxies: Seyfert — galaxies: jets — galaxies: individual (NGC 4151)

1. Introduction

Multi-wavelength high spatial resolution observations of NGC 4151 (e.g., Hutchings et al. 1999; Yang et al. 2001; Mundell et al. 2003; Wang et al. 2009b; Storchi-Bergmann et al. 2009) have provided unique information on the continuum and emission line morphology in the central few 100 pc ($d \sim 13.3$ Mpc, $1'' = 65$ pc, Mundell et al. 1999), contributing to our understanding of the nature of the nuclear emission and its interaction with the host galaxy (see Ulrich 2000 for a review). In this paper we investigate further these topics, using high quality deep *Chandra* ACIS observations of the nearby prototypical Seyfert 1 galaxy NGC 4151, which allow the morphological investigation of spectral line emission in the inner circum-nuclear region ($r \sim 150$ pc in projection). In particular, we will address the radio jet–host galaxy interaction and the nature of the Fe K α line emission.

High resolution radio surveys show broad existence of collimated radio outflows or jets in Seyfert galaxies, albeit less prominent than those of radio galaxies (e.g., Ulvestad & Wilson 1984; Kukula et al. 1995; Nagar et al. 1999; Xanthopoulos et al. 2010). Ever since the *Hubble Space Telescope* emission line imaging resolved the NLR morphology in a number of Seyfert galaxies with linear radio structures (Capetti et al. 1995; Falcke et al. 1998; Cecil et al. 2000), it has been actively debated whether the radio jet plays a competing role against nuclear photoionization in the narrow-line region (NLR) ionization structure (Whittle et al. 1988; Binette et al. 1996; Dopita & Sutherland 1996; Bicknell et al. 1998; Wilson & Raymond 1999; Rossi et al. 2000; Whittle & Wilson 2004; Rosario 2007). *Chandra* X-ray observations of the nuclear regions of nearby Seyfert galaxies appear to offer powerful diagnostics for discriminating between photoionization by the nuclear radiation or collisional ionization by a radio jet (Sako et al. 2000; Young et al. 2001), although the importance of radio jets in shaping NLR environments seems to differ case-by-case (Whittle et al. 2005; Evans et al. 2006; Gandhi et al. 2006; Rosario et al. 2010a,b; Bianchi et al. 2010).

The nuclear region of NGC 4151 is known to host a two-sided, ~ 300 pc-long radio outflow along position angle (P.A.) $\sim 77^\circ$ (e.g., Johnston et al. 1982; Pedlar et al. 1993; Mundell et al. 1995). Within the central 100 pc of the galaxy, Mundell et al. (2003) identified a faint, highly collimated jet underlying discrete components that are shock-like features associated with the jet–gas clouds interactions. Although the distribution of the ionized gas and the kinematics in the NLR imply that shock ionization originated from jet–cloud interactions is unlikely to be the dominant source of ionizing photons compared to the nucleus (Kaiser et al.

2000; Mundell et al. 2003), Mundell et al. (2003) find evidence that some NLR clouds are responsible for bending the jet. Near-IR emission-line mapping of the nuclear region by Storchi-Bergmann et al. (2009) also reveals enhancement of [FeII] emission, suggesting the presence of shock heating in addition to nuclear photoionization (Storchi-Bergmann et al. 2009).

In our previous work using the *Chandra* HRC image of NGC 4151, Wang et al. (2009b) found an excess of X-ray emission at these jet–cloud interaction locations. However, no spectral information could be obtained because of the very limited energy resolution of the HRC. Previous *Chandra* ACIS spectral imaging data of the NGC 4151 nuclear region (Ogle et al. 2000; Yang et al. 2001) were limited by both heavy pile-up¹ and sensitivity, and did not allow detailed high spatial resolution comparison to the radio jet and emission line gas, nor spectral studies of X-ray emission from spatially resolved features. Our 200 ks ACIS-S observation of NGC 4151 (PI Fabbiano; see Wang et al. 2010a, and Wang et al. 2011 for previous work on this data set) allows us to pursue these investigations, by comparing the morphology of the NeIX and OVII with that of the radio jet.

Moreover, with these data we can address the outstanding controversy on the spatial properties of the 6.4 keV Fe K α emission of NGC 4151. In Seyfert galaxies, this emission line is expected to originate from cold matter near the nucleus (< 1 pc), either the obscuring torus (e.g., Krolik & Kallman 1987) or an accretion disk (e.g., George & Fabian 1991; Reynolds 1997). These model predictions, however, conflicted with the finding of Ogle et al. (2000), who reported spatially resolved narrow iron K α line emission in the *Chandra* HETG observation, concluding that $65\% \pm 9\%$ of this emission originates in the ENLR at distance up to $6''$ from the nucleus (~ 400 pc across). This conclusion has been more recently contested by the *XMM-Newton* based work of Schurch et al. (2003).

2. Observations and Data Analysis

The details of our ACIS observations and data reduction are described in Wang et al. (2011, hereafter Paper I). Briefly, NGC 4151 was observed by *Chandra* for a total of 180 ks (after screening for high background intervals) with the spectroscopic array of the Advanced CCD Imaging Spectrometer (ACIS-S; Garmire et al. 2003) in 1/8 sub-array mode during March 27-29, 2008. The data were reprocessed following standard procedures, using CIAO (Version 4.2) with the CALDB 4.2.1 provided by the *Chandra* X-ray Center (CXC). Subpixel event repositioning (“static” method in Li et al. 2004, using the corner split and 2-pixel split

¹See the Chandra ABC Guide to Pileup available at http://cxc.harvard.edu/ciao/download/doc/pileup_abc.pdf

events) and subpixel binning techniques were applied to the ACIS images to improve the spatial resolution.

During our previous work (Wang et al. 2010b) and Paper I, we became well aware of the complexity in data analysis caused by the bright nuclear emission of NGC 4151. First, photon pile-up is present in the nuclear region even with the reduced frame-time of our observation. We established that for the soft X-ray emission, pile-up is moderate ($< 10\%$) at $r > 1''$. Second, although the *Chandra*'s PSF is highly centrally peaked, the contamination from the scattered nuclear emission to the extended emission is not negligible due to the brightness of the nucleus and the broader PSF in the higher energy range. We performed *Chandra* PSF simulations that provide an estimate of the expected contamination from the nuclear emission in an extended feature. Detailed explanation of the analysis leading to these conclusions is presented in Paper I. We have taken into account this information in the following analysis.

2.1. Soft X-ray Emission Line Images

The 2–7 keV emission is dominated by the unresolved nucleus (Yang et al. 2001; Wang et al. 2009b). Since we are interested in the extended X-ray emission, we used the energy range below 2 keV where this emission is prominent (see Paper I). To investigate the general spectral dependency of the morphology of this soft X-ray emission, images in three spectral bands below 2 keV were extracted from the merged data: 0.3–0.7 keV (“soft band”), 0.7–1.0 keV (“medium band”), and 1–2 keV (“hard band”). Following Wang et al. (2009a), exposure maps were created for the individual bands to obtain exposure-corrected flux images.

Figure 1 presents the resulting false color composite image of the central $7'' \times 7''$ (450 pc on a side) region of NGC 4151, where the soft, medium, and hard band images are shown in red, green, and blue, respectively. The images in the three band have been smoothed with a $FWHM = 0.3''$ Gaussian kernel. It clearly shows bright structured soft X-ray emission along the northeast (NE) – southwest (SW) direction, which is also the direction of the radio jet. In particular, the medium band image shows a jet-like $\sim 2''$ linear extension (contours in Figure 1). This medium band is dominated by the NeIX emission (see below). In the following we concentrate on the analysis of this inner $2''$ -radius circum-nuclear region.

High spectral resolution grating spectra of NGC 4151 (Ogle et al. 2000; Schurch et al. 2004; Armentrout et al. 2007) have shown that the emission in these soft spectral bands is almost entirely dominated by lines. Although the spectral resolution of ACIS CCD cannot provide unique identifications of the strongest soft X-ray emission lines (< 2 keV) seen in

the nuclear spectrum (Wang et al. 2010b), we can identify the dominant transitions guided by the HETG observations (Ogle et al. 2000). Most notably the blended lines appear as three strong lines in the ACIS spectrum, approximately centered at 0.57 keV, 0.68 keV, 0.91 keV (c.f. Figure 4 in Yang et al. 2001; Figure 3 in Wang et al. 2010b). We then extracted the X-ray emission in three narrow energy intervals (0.53–0.63 keV, blended OVII f,i,r; 0.63–0.73 keV, blended OVIII Ly α and OVII RRC; 0.85–0.95 keV, blended NeIX f,i,r) to create line strength images, highlighting regions of these prominent emission lines. This is a reasonable approach since the line emission dominates over the weak underlying continuum (Ogle et al. 2000; Schurch et al. 2004) in these narrow bands and reveal substructures that are not obvious in the broadband images (e.g., Bianchi et al. 2010; Gonzalez-Martin et al. 2010).

The resulting images are shown in Figures 2 and 3, showing the X-ray emission-line structure close to the nucleus (the central $r = 2''$, ~ 130 pc) in the context of the radio outflow and the optical emission line clouds. The alignment between these images is done using the peak of X-ray emission, [OIII] emission, and the radio core. Since the astrometry of our *Chandra* image is accurate to $0.3''$, our interpretation of these features is not affected by significant alignment uncertainties. The position of the nucleus is indicated with a cross. The OVII, OVIII, and NeIX emission line images all show extended morphology and some structures, closely following the P.A. of the large scale extended NLR traced by the [OIII] emission (e.g., Winge et al. 1997; Kaiser et al. 2000).

In particular, the linear feature seen in the medium-band is clearly present in the NeIX image. There appears to be two X-ray enhancements bracketed by the optical clouds (indicated by arrows in Figure 3) that are close to the radio knot features C2 and C5 (Mundell et al. 1995). These “hot spots” are better visualized in the NeIX/OVII ratio image, shown in Figure 4 together with the VLBA jet (Mundell et al. 2003) and the NIR [FeII] line emission (Storchi-Bergmann et al. 2009). The locations where the jet appears to be intercepted by the optical clouds and where prominent [FeII] emission arise, are characterised by a NeIX/OVII ratio of 2.8 ± 0.2 , which is significantly ($\sim 6\sigma$) higher than the ratio in the surrounding regions (1.2 ± 0.2). We also examined the optical clouds with high velocity dispersion, possibly associated with jet-cloud impact (marked as crosses in Figure 4; see Figure 7 in Mundell et al. 2003), and find an elevated NeIX/OVII ratio of 2.1 ± 0.4 (with marginal significance). The eastern NeIX/OVII hot spot appears to be associated with clear interactions between the jet and the gas cloud, where shock heating becomes important. We note that the observed line flux of OVII is more suppressed than NeIX in the presence of the Galactic absorption column ($N_H = 2 \times 10^{20}$ cm $^{-2}$), and XSPEC (Arnaud 1996) simulations show the absorption corrected ratio may systematically decrease by 10%. Thus the presence of NeIX/OVII hot spots is not affected, unless there is significant differential absorption in

the region.

2.2. Spectral Analysis of the Soft Emission

We extracted X-ray spectra from both the high NeIX/OVII emission line ratio regions and the surrounding low ratio region (Figure 4b), and fit them jointly (with the same model components but normalizations set free) for comparison using XSPEC (Version 12.5; Arnaud 1996). Spectra and instrument responses were generated using CIAO tool *specextract*². The background spectrum is taken from a nearby source-free region on the same CCD node. Spectra were grouped to have a minimum of 20 counts per energy bin to allow for χ^2 fitting. The contribution from the bright nuclear emission cannot be neglected here; to have a self-consistent model, we included a fraction of the scattered emission predicted from the PSF simulation of the point-like NGC 4151 nucleus.

We have made use of the `Cloudy` photoionization modeling code, last described by Ferland et al. (1998), to model the soft X-ray emission. Using `Cloudy` version C08.00³, which enables a `Cloudy`/XSPEC interface (Porter et al. 2006), we attempted to produce the soft part of the X-ray spectrum assuming an open plane-parallel geometry (“slab”). The dimensionless ionization parameter (Osterbrock & Ferland 2006) is defined as $U = Q/(4\pi r^2 c n_H)$, where n_H is the hydrogen number density, r is the distance to the inner face of the model slab, c is the speed of light, and $Q = \int_{13.6\text{eV}}^{\infty} L_\nu/h\nu$ is the emitting rate of hydrogen ionizing photons (s^{-1}) by the ionizing source. It was previously noted that the spectral fit to the soft X-ray continuum of the nucleus is quite uncertain because of heavy absorption (Armentrout et al. 2007), therefore we adopted the broken power-law form in Kraemer et al. (2005) for the AGN continuum ($\text{Gamma} = 2.3$ for the energy range between 13.6 eV and 0.5 keV, and $\text{Gamma} = 1.5$ for $E > 0.5$ keV). Normalizing to the observed X-ray luminosity of the nucleus (Wang et al. 2010b), we obtain $Q \sim 7 \times 10^{53}$ (photons s^{-1}). We varied U and the column density N_H of the model slab to create spectral model grids, which were fed to XSPEC.

We quickly find that, using a single photoionized component alone cannot reproduce the observed soft X-ray emission in NGC 4151. With a high photoionization component ($\log U \sim 1.9$), we were able to produce the hydrogen-like neon and oxygen lines emission (e.g., OVIII, NeX), which are unambiguously present in all the grating spectra (e.g., Ogle et al.

²<http://cxc.harvard.edu/ciao/threads/specextract/>

³Available at <http://www.nublado.org/wiki/Download>

2000; Schurch et al. 2004; Armentrout et al. 2007). However, the helium-like transitions, in particular the OVII and NeIX emission line features, are not fitted acceptably. Adding a second lower ionization photoionized component ($\log U \sim 0$), as detected in Armentrout et al. (2007), we were able to obtain a significantly improved fit ($\Delta\chi = 200$), except for residuals in the 0.7–1.1 keV range that are particularly strong for the hot spot spectrum. Adding additional photoionized components to the model does not further improve the fit when an F-test is performed. Allowing different absorption columns for the models also does not give a better fit (reduced $\chi^2_\nu = 1.7$), indicating that the high NeIX/OVII ratio is not due to higher obscuration. The absorption column required by the fits is consistent with the low Galactic extinction towards the NLR region found in Crenshaw & Kraemer (2005). Instead, these residuals disappear when a thermal emission component (*APEC*; Smith et al. 2001) with a temperature of $kT = 0.58 \pm 0.05$ keV is added to the model, suggesting the presence of collisionally ionized Fe L emission. The spectral fitting results are summarized in Table 1 and shown in Figure 5. The absorption column is consistent with the low Galactic extinction towards the NLR region found in Crenshaw & Kraemer (2005).

Lastly, we note that fitting the data with only combinations of absorbed optically-thin thermal emission (*APEC*) gave strong residuals of emission line features (reduced $\chi^2_\nu \gg 1$), even when the abundance Z is allowed to vary.

2.3. [OIII]/Soft X-ray Ratios in the Substructures

The subpixel resolution ACIS image also allows a similar comparison of the X-ray emission with the optical NLR clouds resolved in the *HST* image. Taking advantage of the spectral capability of ACIS, we measured the 0.3–2 keV counts for the same [OIII] clouds identified in Wang et al. (2010b), and derived their 0.5–2 keV X-ray fluxes using the spectral model above. To subtract the nuclear contribution, we used a local region at the same radii but with different azimuthal angles than the clouds. The results are listed in Table 2. Figure 6 shows these [OIII] to soft X-ray ratios, comparing the measurements with HRC results in Wang et al. (2010b) and photoionization models in Bianchi et al. (2006).

The [OIII]/X-ray ratios at the two X-ray hot spot locations (corresponding to radio knots C2 and C5 in Mundell et al. 1995) were also measured, and found to be uniformly low, ~ 3 . This was previously noted in Wang et al. (2009b), and implies enhanced X-ray emission compared to other clouds under nuclear photoionization, which is likely associated with the jet–cloud interaction and consistent with their association with high NeIX/OVII ratio regions.

2.4. Spatial Morphology of the Fluorescent Line Emission

The 6.4 keV fluorescent iron $K\alpha$ emission of neutral or mildly ionized cold material is readily visible in the ACIS spectra of the nucleus (Wang et al. 2010b) and the extended region (Figure 7a). Another fluorescent feature, SiI $K\alpha$ emission at 1.74 keV, is also clearly present in the extended emission (Figure 7b). Both spectra of extended emission were extracted from a $2'' < r < 30''$ annular region centered on the nucleus. Is this “extended” fluorescent line emission truly originating from outside the nuclear region, or is it the result of the PSF wing spreading out point-like nuclear features?

To determine the spatial distribution of the Fe $K\alpha$ line emitting material, we followed the procedure in Smith & Wilson (2001): a continuum image, taken to be the average of the counts in the 5.9–6.2 keV and 6.5–6.8 keV bands, was subtracted from the image extracted in the 6.2–6.5 keV band, resulting in a “pure” Fe $K\alpha$ line image, shown in Figure 8a. The Fe $K\alpha$ emission appears mostly circular in the $r \leq 2''$, but shows faint extended emission towards the north and west.

The Si $K\alpha$ line is blended with the MgXII $Ly\beta$ and SiXIII f, r emission (Ogle et al. 2000), thus the above continuum subtraction is not applied. We extracted emission in the 1.7–1.8 keV range to obtain the Si $K\alpha$ emission map (Figure 8b). It is mostly concentrated within a $r \sim 2''$ circle, with a slight elongation along the optical bi-cone direction (northeast–southwest).

However, at such energies the wings of the energy-dependent telescope PSF spread a small but non-negligible amount of the nuclear photons to large radii. Thus the presence of “extended” Fe $K\alpha$ emission or Si $K\alpha$ emission in the $r > 1''$ region may in fact come from the PSF-scattered unresolved nuclear emission.

To investigate this point, we further compared the observed radial profile of the Fe $K\alpha$ emission band (6.2–6.5 keV) and the radial profile in the same band for a point-like nucleus simulated with MARX⁴ (see Wang et al. 2010b), shown in Figure 9a. A similar comparison for the Si $K\alpha$ (1.7–1.8 keV) is shown in Figure 9b. The extracted observed profiles shown in Figure 9 agree well with the PSF profiles, except for the inner $r < 2''$ where the simulation overpredicted the observed emission due to heavy pile up in the PSF core.

The simulated PSFs indicate that the $r \leq 2''$ region contains 89% of the point source emission in the 6.2–6.5 keV band and 94% of the point source emission in the 1.7–1.8 keV band. Approximately 6% of the nuclear Fe $K\alpha$ emission is expected to be spread within the

⁴Available at <http://space.mit.edu/CXC/MARX/>

$2'' \lesssim r \lesssim 6''$ extended regions, the extent of Fe $K\alpha$ seen in Figure 7a. Taking into account the contribution from the PSF wings, the remaining extended Fe $K\alpha$ emission is $5 \pm 1\%$ of the total Fe $K\alpha$ emission. This should be considered an upper limit for the truly extended emission, because the nuclear Fe $K\alpha$ emission is likely to be underestimated due to pile up. Similarly, we estimated that the extended Si $K\alpha$ emission is $\lesssim 4 \pm 1\%$ of the total Si $K\alpha$ emission. As pointed out by the referee, the measured extended emission could easily disappear with a slightly broader simulated PSF given that the DitherBlur parameter in the MARX simulation is not known a priori.

Therefore, we conclude that although there is faint extended emission seen in the Fe and Si fluorescent line images, at most 5% of the observed Fe $K\alpha$ emission and 4% of the Si $K\alpha$ emission can be truly spatially extended; most of these emissions are consistent with the PSF scattering of a strong nuclear component.

3. Discussion

3.1. Jet–Cloud Interaction in a Photoionized Outflow

Both our previous work using HRC image of NGC 4151 nuclear region (Wang et al. 2009b) and this work using ACIS find that most of the NLR clouds in the central 150 pc radius region of NGC 4151 have a relatively constant [OIII] to soft X-ray ratio (~ 10 ; Figure 6 and Table 2), no matter the distance of the clouds from the nucleus. This ratio indicates a uniform ionization parameter and a density decreasing as r^{-2} . This may be consistent with a photoionized wind scenario (e.g., Bianchi et al. 2006) as the NLR clouds are outflowing (e.g., Kaiser et al. 2000). The [OIII]/X-ray ratios at the locations of jet-cloud collision are lower (~ 3), leading to the suggestion of enhanced X-ray emission in these regions due to shock heating in addition to photoionization.

This conclusion is supported by the results of multiwavelength imaging studies. The high spatial resolution emission line images of OVII, OVIII, and NeIX emission show extended structures, in particular two “hot spots” in the NeIX image, which are close to the radio knot features (Figures 2 and 3). At these locations ($1''$ from the nucleus), Mundell et al. (2003) noted that the morphology of the highly collimated radio outflows appears more disturbed, suggesting interaction with some dense clouds here. There are also clearly optical clouds with high velocity dispersion associated with the jet–cloud impact (Mundell et al. 2003). The radio knots are near to the location of strong [FeII] emission (Storchi-Bergmann et al. 2009), falling between the peaks of the [FeII] emission.

Altogether, the morphology suggests a scenario where the radio ejecta runs into a

denser cloud in the inhomogeneous ISM and results in locally enhanced shock heating (e.g., Capetti et al. 1999). This jet–cloud interaction has been suggested to explain the enhanced [FeII] emission, which could be due to the iron unlocked from grains by the shocks (Storchi-Bergmann et al. 2009). The NeIX emission, which traces the higher ionization gas, becomes more prominent with the extra collisional ionization from the jet–cloud interaction. Armentrout et al. (2007) also noted that the poor fit to the OVII line profile in the grating spectra could be due to presence of a non-photoionization component. This possibility is further supported by our spectral fits, which suggest that the NeIX/OVII enhancements have a thermal origin, requiring the presence of a collisionally ionized plasma (the $kT = 0.58 \pm 0.05$ keV component) in addition to a photoionized nuclear outflow (Yang et al. 2001; Wang et al. 2009b).

The emission measure of the *APEC* component allows us to estimate the electron density n_e ($\approx n_H$) and the thermal pressure p_{th} ($\sim 2n_e kT$). The emitting volume (V) of the hot gas, assuming that the depth along the line of sight is comparable to the other dimensions, is 5.6×10^{60} cm³ for the high NeIX/OVII ratio hot spots. The filling factor η is assumed to be 100% and both of n_e and p_{th} have a weak dependence on η ($p \propto \eta^{-1/2}$). There is $\sim 10\%$ uncertainty in kT , which is propagated to the estimated pressure and energy. For the $kT = 0.58$ keV emission, we derived an average density $n_e = 0.06$ cm⁻³, a hot gas pressure $p_{th} = 6.8 \times 10^{-10}$ dyne cm⁻², a thermal energy content of $E_{th} = 4 \times 10^{51}$ ergs, and a cooling time of $\tau_c = E_{th}/L_{APEC} \sim 10^5$ yr. The estimated internal pressure of the radio jet based on the synchrotron minimum energy assumption ranges between 10^{-7} and 10^{-9} dyne cm⁻² (Pedlar et al. 1993), to be confined by the hot gas pressure of 10^{-9} dyne cm⁻², which further supports our collisional ionization scenario.

Assuming $T = 10^4$ K for the photoionized clouds and $n_e = 220$ cm⁻³ (Penston et al. 1990), the thermal pressure from the photoionized gas is $p_{ph} = 3 \times 10^{-10}$ dyne cm⁻², which is comparable to the thermal pressure of the hot ISM, implying a possible pressure equilibrium between the collisionally ionized hot gas and the photoionized line-emitting cool clouds.

We further estimate the age of the interaction from the approximate crossing time of the 0.5'' region (dimension of the radio knot; Pedlar et al. 1993) with a characteristic velocity of $c_s = 200$ km s⁻¹, the local sound speed. This is approximately the thermal velocity for the 0.58 keV gas ($v_{th} = 240$ km s⁻¹), and also at the order of velocity dispersion of emission line gas seen in Storchi-Bergmann et al. (2010). Assuming the strong shock jump conditions, a crude estimate of the shock velocity v_{sh} can be obtained using $T \approx 1.5 \times 10^5$ K $(v_{sh}/100 \text{ km s}^{-1})^2$ (Raga et al. 2002). For the $T \sim 6.7 \times 10^6$ K X-ray-emitting gas, a v_{sh} of ~ 700 km s⁻¹ relative to the downstream material is required. This appears consistent with a supersonic but relatively slow radio jet, which is constrained to be sub-relativistic from

radio proper motion estimates (e.g., $v_{jet} < 12000 \text{ km s}^{-1}$; Ulvestad et al. 2005). Thus we obtain a characteristic timescale of $t_{cross} \sim 10^5 \text{ yr}$.

If the jet–cloud interaction converts kinematic energy into heating of the hot gas, a lower limit can be placed on the kinematic luminosity of the jet, $L_{K.E.} \gtrsim E_{th}/t_{cross} = 1 \times 10^{39} \text{ erg s}^{-1}$. It is interesting to compare this observed $L_{K.E.}$ to the jet power directly inferred from the synchrotron emission. Using the P_{jet} – P_{radio} scaling relation (Equation 1) in Cavagnolo et al. (2010) and a total radio luminosity at 1.4 GHz ($\nu L_\nu \approx 4 \times 10^{37} \text{ erg s}^{-1}$; Mundell et al. 1999), we find $P_{jet} \sim 10^{42} \text{ erg s}^{-1}$, suggesting that $\gtrsim 0.1\%$ of the jet power is deposited in the ISM. However, recalling that the P_{jet} – P_{radio} relation was derived from a sample of radio loud galaxies with X-ray cavities (see Cavagnolo et al. 2010 for review on the P_{jet} – P_{radio} scaling relation) while here NGC 4151 is of low radio power, we also estimate directly the jet energy flux using the pressure in the knots (Pedlar et al. 1993) based on the minimal energy assumption, giving a similar $P_{jet} = 5 \times 10^{42} \text{ erg s}^{-1}$.

We further note that, the crossing time t_{cross} is comparable to the cooling time τ_c , implying that the hot gas is prominent only locally (close to the radio knots). Indeed, along the path of the radio jet, the clouds that are spatially close to the jet impact spots (e.g., clouds #3,4 bracketing knot C2; #9,10 for knot C5) show [OIII]/X-ray ratios indistinguishable from others (Figure 6). If these clouds are physically related to the ISM interacting with the jet, instead of being projected close to the knots in our line-of-sight, their X-ray emission shows little evidence for excess shock heating in addition to nuclear photoionization. This localized heating is perhaps related to the highly collimated radio ejecta in NGC 4151 (Mundell et al. 2003), in contrast to the more expanded lobe-like radio outflow in Mrk 3 (Capetti et al. 1999), where the NLR gas appears broadly impacted. We plan to investigate in future work whether the [OIII]/X-ray ratio, such as $\lesssim 4$ measured here and seen in Mrk 3 and NGC 1386 (Bianchi et al. 2006), together with other line ratios (e.g., [FeII]/[PII]; Oliva et al. 2001) could be useful diagnostics for strong jet–ISM interaction in Seyfert galaxies.

In terms of energetics, we summarize our findings in NGC 4151: (a) The jet power estimated from the radio power is $\sim 10^{42} \text{ erg s}^{-1}$, a few percent of the current AGN energy output ($L_{bol} = 7 \times 10^{43} \text{ erg s}^{-1}$; Kaspi et al. 2005), which is close to the canonical $\sim 5\%$ of the radiant energy adopted in theoretical models for efficient AGN feedback (e.g., Di Matteo et al. 2005; Hopkins et al. 2006); (b) $\gtrsim 0.1\%$ of the jet power is observed to have been deposited into the host ISM in the nuclear region through the interaction between the radio jet and the dense medium; (c) The shock heating due to the jet–cloud interaction appears localized to the impact spots, and most clouds are consistent with being photoionized by the nucleus.

3.2. Extent and Origin of the Fe K α Line

Ogle et al. (2000) claimed that the narrow iron line emission was spatially resolved in the *Chandra* HETG observation and $65\% \pm 9\%$ of the FeI K α emission comes from the ENLR at distance up to $6''$ extent (~ 400 pc across). This is intriguing, since the putative pc-scale torus or more compact broad-line region (Liu et al. 2010, and references therein) are expected to be the primary location of narrow FeI K α emission. Schurch et al. (2003) cautioned that due to the sensitivity of the short grating observation in Ogle et al. (2000), the 1–3 arcsec region off the peak of cross-dispersion profile contains few photons. Therefore the detection of spatially extended iron line emission cannot be significant. A high signal-to-noise XMM-Newton spectrum of the neutral Fe K α suggests that all line flux originates in a nearly Compton-thick torus that is not resolvable at current resolution (Schurch & Warwick 2002; Schurch et al. 2003).

Our results show that the extended Fe K α emission, if present, is only at $\sim 5\%$ level of the observed Fe K α emission, when the contribution from the PSF wings is taken into account. This is consistent with our constraint on the extent of the Si fluorescent emission and supports the conclusions of Schurch et al. (2003), while it is in strong disagreement with the 65% reported in Ogle et al. (2000). We note that in Ogle et al. (2000) the PSF is represented as a narrow Gaussian with $FWHM = 0.9''$, when the *Chandra* mission was new. The MARX model is now much more advanced so that a more reliable estimate becomes possible. At 6.4 keV, the encircled energy fraction of a point source is only 63.7% (see *Chandra* Proposers' Observatory Guide⁵ Chapter 4 Table 4.2) in such a PSF core. Hence a significant fraction of the nuclear emission could have been measured in Ogle et al. as spatially extended Fe K α emission.

4. Conclusions

In this paper we present spectral analysis and emission line images from deep *Chandra* observation of NGC 4151, aiming to resolve and characterise the X-ray emission in the inner ~ 130 pc-radius nuclear region. The findings are summarized as follows:

1. We have obtained high spatial resolution X-ray narrow-band images of OVII, OVIII, and NeIX line emission, which are blended at the ACIS spectral resolution. The images show extended structures that are spatially correlated with the radio outflow

⁵<http://cxc.harvard.edu/proposer/POG/>

and optical [OIII] emission.

2. We find strong evidence for jet–ISM interaction, including morphological correspondences with regions of X-ray enhancement, peaks of NIR [FeII] emission, and optical clouds. This is further strengthened by the presence of a $kT = 0.58$ keV collisionally ionized component in the spectral fitting of the hot spots, and by the excess of X-ray emission in addition to nuclear photoionization as indicated by a low [OIII]/X-ray ratio. We find a possible pressure equilibrium between the collisionally ionized hot gas and the photoionized cool clouds. The estimated velocity of the shocks from the jet–cloud impact is ~ 700 km s⁻¹.
3. We estimate that the jet power in NGC 4151 is close to a few percent of the current AGN energy output ($L_{bol} \sim 7 \times 10^{43}$ erg s⁻¹). The derived thermal energy in the hot gas suggests that $\gtrsim 0.1\%$ of the jet power is deposited into the host ISM in the nuclear region through the interaction between the radio-jet and the dense medium. The [OIII]/X-ray ratios of NLR clouds bracketing the radio knots show little deviation from other photoionized clouds, indicating a localized impact on the ISM by the highly collimated jet.
4. We investigate the spatial extent of the fluorescent features, including the Fe K α emission and the Si K α emission. Our results show that both are dominated by point-like emission, consistent with an origin of unresolved inner structure such as a torus. The extended Fe K α emission is $\lesssim 5\%$ of the observed Fe K α emission, which is in strong disagreement with the 65% reported in Ogle et al. (2000).

We thank the anonymous referee for helpful suggestions. This work is supported by NASA grant GO8-9101X (PI: Fabbiano) and grant GO1-12009X (PI: Wang). We acknowledge support from the CXC, which is operated by the Smithsonian Astrophysical Observatory (SAO) for and on behalf of NASA under Contract NAS8-03060. CGM acknowledges financial support from the Royal Society and Research Councils U.K. J. W. thanks G. Ferland, T. Kallman, S. Bianchi, A. Marinucci, and S. Chakravorty for extensive advices on photoionization modeling, P. Nulsen for jet power discussion, T. Storchi-Bergmann and R. Riffel for providing the Gemini NIFS maps. This research has made use of data obtained from the *Chandra* Data Archive, and software provided by the CXC in the application packages CIAO and Sherpa.

Facilities: CXO (HRC, ACIS)

REFERENCES

- Armentrout, B. K., Kraemer, S. B., & Turner, T. J. 2007, *ApJ*, 665, 237
- Arnaud, K. A. 1996, *Astronomical Data Analysis Software and Systems V*, 101, 17
- Bianchi, S., Chiaberge, M., Evans, D. A., Guainazzi, M., Baldi, R. D., Matt, G., & Piconcelli, E. 2010, *MNRAS*, 405, 553
- Bianchi, S., Guainazzi, M., & Chiaberge, M. 2006, *A&A*, 448, 499
- Bicknell, G. V., Dopita, M. A., Tsvetanov, Z. I., & Sutherland, R. S. 1998, *ApJ*, 495, 680
- Binette, L., Wilson, A. S., & Storchi-Bergmann, T. 1996, *A&A*, 312, 365
- Capetti, A., Axon, D. J., Kukula, M., Macchetto, F., Pedlar, A., Sparks, W. B., & Boksenberg, A. 1995, *ApJ*, 454, L85+
- Capetti, A., Axon, D. J., Macchetto, F. D., Marconi, A., & Winge, C. 1999, *ApJ*, 516, 187
- Cavagnolo, K. W., McNamara, B. R., Nulsen, P. E. J., Carilli, C. L., Jones, C., & Bîrzan, L. 2010, *ApJ*, 720, 1066
- Cecil, G., et al. 2000, *ApJ*, 536, 675
- Crenshaw, D. M., & Kraemer, S. B. 2005, *ApJ*, 625, 680
- Di Matteo, T., Springel, V., & Hernquist, L. 2005, *Nature*, 433, 604
- Dopita, M. A., & Sutherland, R. S. 1996, *ApJS*, 102, 161
- Evans, D. A., Lee, J. C., Kamenetska, M., Gallagher, S. C., Kraft, R. P., Hardcastle, M. J., & Weaver, K. A. 2006, *ApJ*, 653, 1121
- Falcke, H., Wilson, A. S., & Simpson, C. 1998, *ApJ*, 502, 199
- Ferland, G. J., Korista, K. T., Verner, D. A., Ferguson, J. W., Kingdon, J. B., & Verner, E. M. 1998, *PASP*, 110, 761
- Gandhi, P., Fabian, A. C., & Crawford, C. S. 2006, *MNRAS*, 369, 1566
- Garmire, G. P., Bautz, M. W., Ford, P. G., Nousek, J. A., & Ricker, Jr., G. R. 2003, in *Society of Photo-Optical Instrumentation Engineers (SPIE) Conference Series*, Vol. 4851, *Society of Photo-Optical Instrumentation Engineers (SPIE) Conference Series*, ed. J. E. Truemper & H. D. Tananbaum, 28–44

- George, I. M., & Fabian, A. C. 1991, MNRAS, 249, 352
- Gonzalez-Martin, O., Acosta-Pulido, J. A., Perez Garcia, A. M., & Ramos Almeida, C. 2010, ApJ, 723, 1748
- Hopkins, P. F., Hernquist, L., Cox, T. J., Di Matteo, T., Robertson, B., & Springel, V. 2006, ApJS, 163, 1
- Hutchings, J. B., et al. 1999, AJ, 118, 2101
- Johnston, K. J., Elvis, M., Kjer, D., & Shen, B. S. P. 1982, ApJ, 262, 61
- Kaiser, M. E., et al. 2000, ApJ, 528, 260
- Kaspi, S., Maoz, D., Netzer, H., Peterson, B. M., Vestergaard, M., & Jannuzi, B. T. 2005, ApJ, 629, 61
- Kraemer, S. B., et al. 2005, ApJ, 633, 693
- Krolik, J. H., & Kallman, T. R. 1987, ApJ, 320, L5
- Kukula, M. J., Pedlar, A., Baum, S. A., & O’Dea, C. P. 1995, MNRAS, 276, 1262
- Li, J., Kastner, J. H., Prigozhin, G. Y., Schulz, N. S., Feigelson, E. D., & Getman, K. V. 2004, ApJ, 610, 1204
- Liu, Y., et al. 2010, ApJ, 710, 1228
- Mundell, C. G., Pedlar, A., Baum, S. A., O’Dea, C. P., Gallimore, J. F., & Brinks, E. 1995, MNRAS, 272, 355
- Mundell, C. G., Pedlar, A., Shone, D. L., & Robinson, A. 1999, MNRAS, 304, 481
- Mundell, C. G., Wrobel, J. M., Pedlar, A., & Gallimore, J. F. 2003, ApJ, 583, 192
- Murphy, E. M., Lockman, F. J., Laor, A., & Elvis, M. 1996, ApJS, 105, 369
- Nagar, N. M., Wilson, A. S., Mulchaey, J. S., & Gallimore, J. F. 1999, ApJS, 120, 209
- Ogle, P. M., Marshall, H. L., Lee, J. C., & Canizares, C. R. 2000, ApJ, 545, L81
- Oliva, E., et al. 2001, A&A, 369, L5
- Osterbrock, D. E., & Ferland, G. J. 2006, Astrophysics of gaseous nebulae and active galactic nuclei (University Science Books)

- Pedlar, A., Kukula, M. J., Longley, D. P. T., Muxlow, T. W. B., Axon, D. J., Baum, S., O’Dea, C., & Unger, S. W. 1993, *MNRAS*, 263, 471
- Penston, M. V., et al. 1990, *A&A*, 236, 53
- Porter, R. L., Ferland, G. J., Kraemer, S. B., Armentrout, B. K., Arnaud, K. A., & Turner, T. J. 2006, *PASP*, 118, 920
- Raga, A. C., Noriega-Crespo, A., & Velázquez, P. F. 2002, *ApJ*, 576, L149
- Reynolds, C. S. 1997, *MNRAS*, 286, 513
- Rosario, D. J., Whittle, M., Nelson, C. H., & Wilson, A. S. 2010a, *MNRAS*, 408, 565
- . 2010b, *ApJ*, 711, L94
- Rosario, D. J. V. 2007, PhD thesis, University of Virginia
- Rossi, P., Capetti, A., Bodo, G., Massaglia, S., & Ferrari, A. 2000, *A&A*, 356, 73
- Sako, M., Kahn, S. M., Paerels, F., & Liedahl, D. A. 2000, *ApJ*, 543, L115
- Schurch, N. J., & Warwick, R. S. 2002, *MNRAS*, 334, 811
- Schurch, N. J., Warwick, R. S., Griffiths, R. E., & Kahn, S. M. 2004, *MNRAS*, 350, 1
- Schurch, N. J., Warwick, R. S., Griffiths, R. E., & Sembay, S. 2003, *MNRAS*, 345, 423
- Smith, D. A., & Wilson, A. S. 2001, *ApJ*, 557, 180
- Smith, R. K., Brickhouse, N. S., Liedahl, D. A., & Raymond, J. C. 2001, *ApJ*, 556, L91
- Storchi-Bergmann, T., Lopes, R. D. S., McGregor, P. J., Riffel, R. A., Beck, T., & Martini, P. 2010, *MNRAS*, 402, 819
- Storchi-Bergmann, T., McGregor, P. J., Riffel, R. A., Simões Lopes, R., Beck, T., & Dopita, M. 2009, *MNRAS*, 394, 1148
- Ulrich, M. 2000, *A&A Rev.*, 10, 135
- Ulvestad, J. S., & Wilson, A. S. 1984, *ApJ*, 285, 439
- Ulvestad, J. S., Wong, D. S., Taylor, G. B., Gallimore, J. F., & Mundell, C. G. 2005, *AJ*, 130, 936

- Wang, J., Fabbiano, G., Karovska, M., Elvis, M., Risaliti, G., Zezas, A., & Mundell, C. G. 2009a, *ApJ*, 704, 1195
- Wang, J., Fabbiano, G., Elvis, M., Risaliti, G., Mazzarella, J. M., Howell, J. H., & Lord, S. 2009b, *ApJ*, 694, 718
- Wang, J., Fabbiano, G., Risaliti, G., Elvis, M., Mundell, C. G., Dumas, G., Schinnerer, E., & Zezas, A. 2010a, *ApJ*, 719, L208
- Wang, J., Risaliti, G., Fabbiano, G., Elvis, M., Zezas, A., & Karovska, M. 2010b, *ApJ*, 714, 1497
- Wang, J., et al. 2011, *ApJ*, 729, 75
- Whittle, M., Pedlar, A., Meurs, E. J. A., Unger, S. W., Axon, D. J., & Ward, M. J. 1988, *ApJ*, 326, 125
- Whittle, M., Rosario, D. J., Silverman, J. D., Nelson, C. H., & Wilson, A. S. 2005, *AJ*, 129, 104
- Whittle, M., & Wilson, A. S. 2004, *AJ*, 127, 606
- Wilson, A. S., & Raymond, J. C. 1999, *ApJ*, 513, L115
- Winge, C., Axon, D. J., Macchetto, F. D., & Capetti, A. 1997, *ApJ*, 487, L121+
- Xanthopoulos, E., Thean, A. H. C., Pedlar, A., & Richards, A. M. S. 2010, *MNRAS*, 404, 1966
- Yang, Y., Wilson, A. S., & Ferruit, P. 2001, *ApJ*, 563, 124
- Young, A. J., Wilson, A. S., & Shopbell, P. L. 2001, *ApJ*, 556, 6

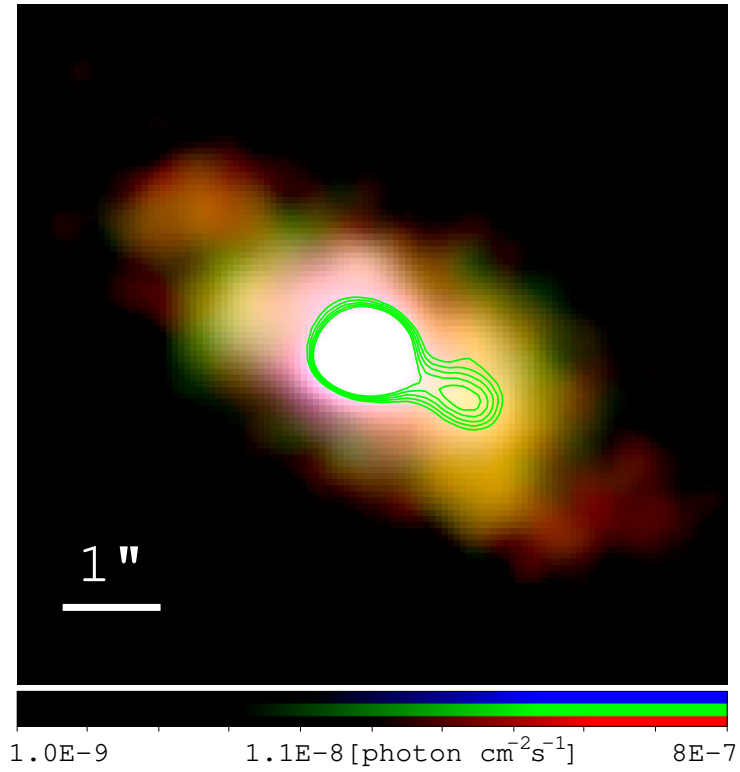


Fig. 1.— The tri-color composite image of the central $7'' \times 7''$ (450 pc-across) circumnuclear region of NGC 4151, where the soft (0.3–0.7 keV), medium (0.7–1 keV), and hard band (1–2 keV) images have been smoothed with a $FWHM = 0.3''$ Gaussian kernel and shown in red, green, and blue, respectively. The contours are of the medium band and highlight a linear feature spatially coincident with the radio jet. The pixel scale is $0.0625''$ per pixel, 1/8 the native ACIS pixel.

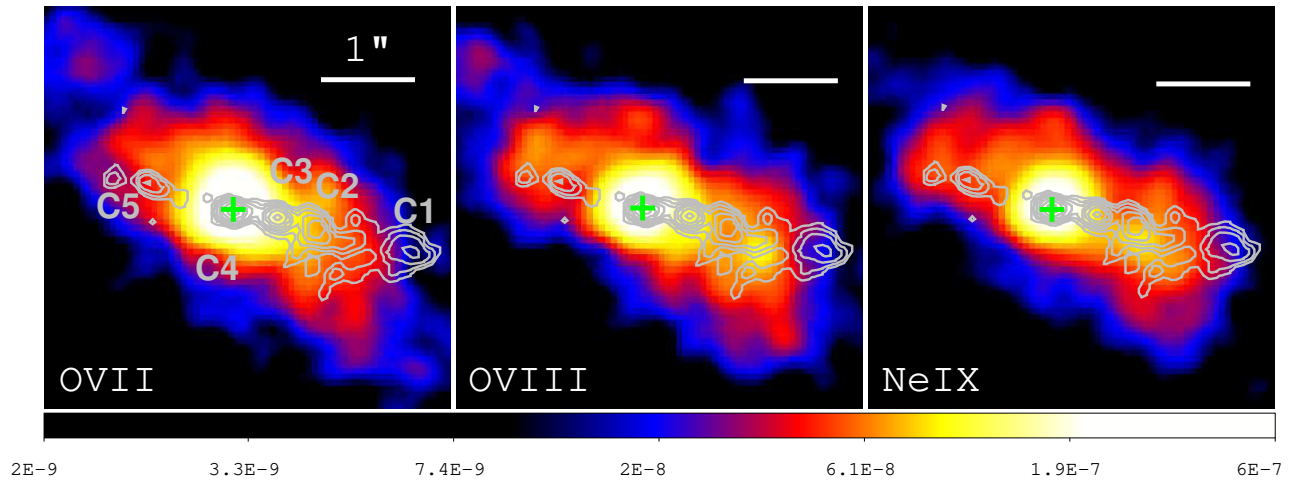


Fig. 2.— The emission-line structure of the hot ISM in the central ~ 250 pc of NGC 4151 (a) OVII; (b) OVIII+OVII RRC; (c) NeIX. The nucleus position is indicated with a cross. The contours outline the radio outflow in the 1.4 GHz MERLIN map (Mundell et al. 1995). The ACIS images have been rebinned to $0.0625''$ per pixel, and smoothed with a $FWHM = 0.3''$ Gaussian kernel.

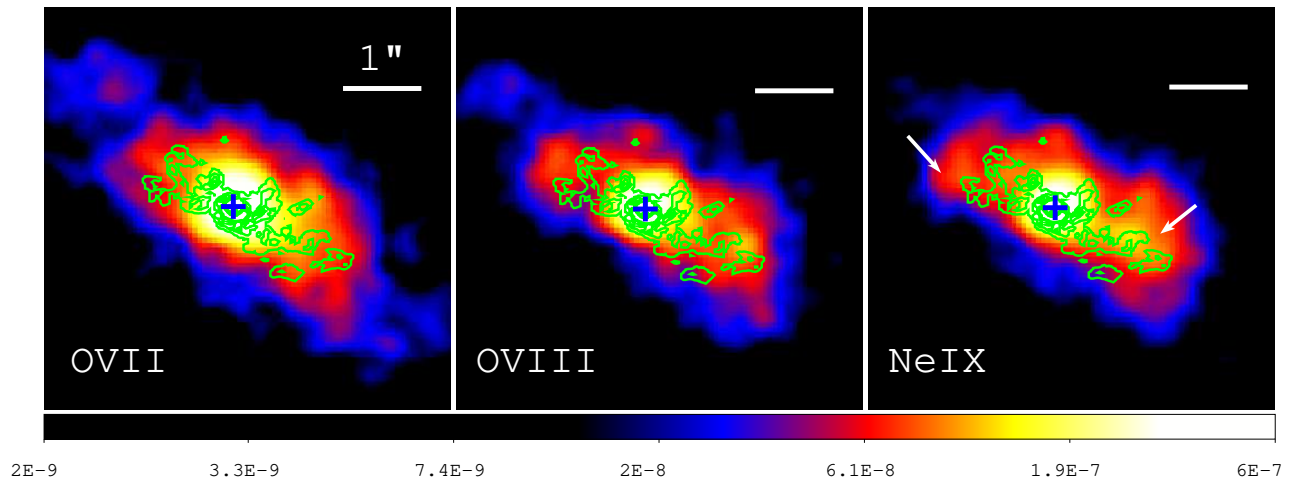


Fig. 3.— Same emission-line maps of the central ~ 250 pc of NGC 4151 as in Figure 2, but with contours showing the *HST*/FOC [OIII] $\lambda 5007$ emission line clouds (Winge et al. 1997). (a) OVII; (b) OVIII+OVII RRC; (c) NeIX. The ACIS images have been rebinned to $0.0625''$ per pixel, and smoothed with a $FWHM = 0.3''$ Gaussian kernel.

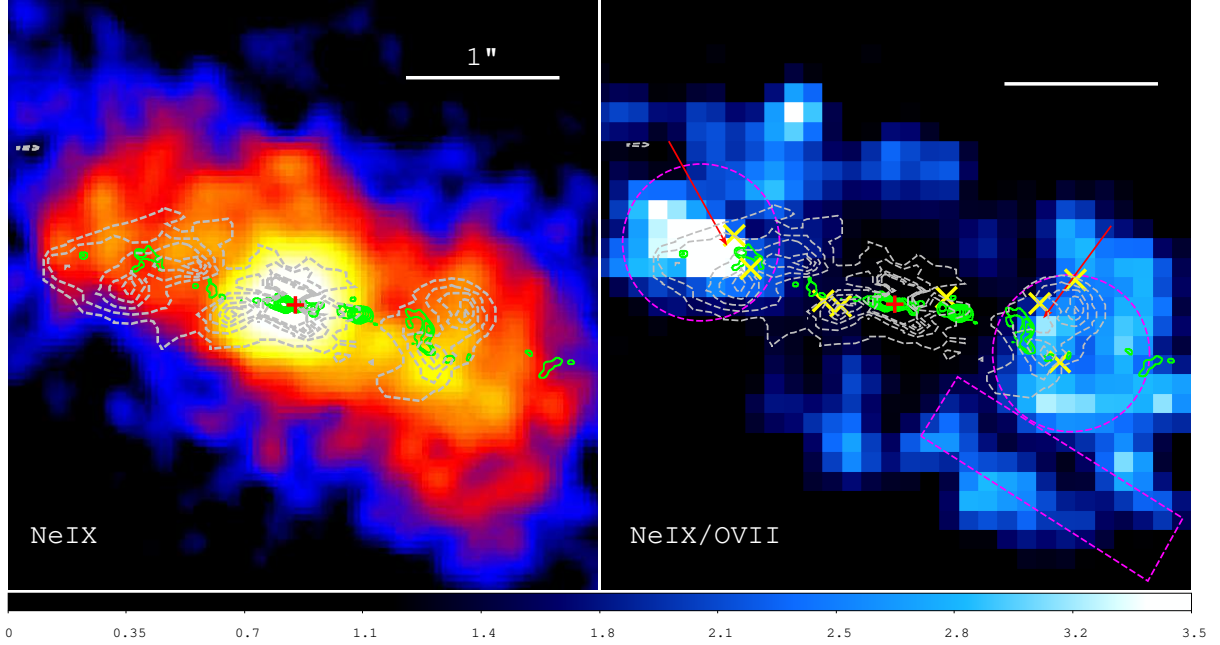


Fig. 4.— (a) A close view of the NeIX emission line image overlaid with the contours of VLBA+VLA radio jet (green lines, Mundell et al. 2003) and NIR [FeII] (black dashed lines; Storchi-Bergmann et al. (2009)). Note how the NeIX line emission peaks appears to align with the general direction of the linear radio outflow. (b) Ratio image between the NeIX band and the OVII band images. Contours are the same as in (a). The arrows (red) indicate the knots of high NeIX/OVII ratios, and the circles (magenta) mark the spectra extraction regions. The box (magenta) marks the extraction region for the low NeIX/OVII ratio region. The crosses (yellow) mark the locations of the *HST* clouds with high velocity dispersion (Kaiser et al. 2000; see also Figure 7 in Mundell et al. 2003).

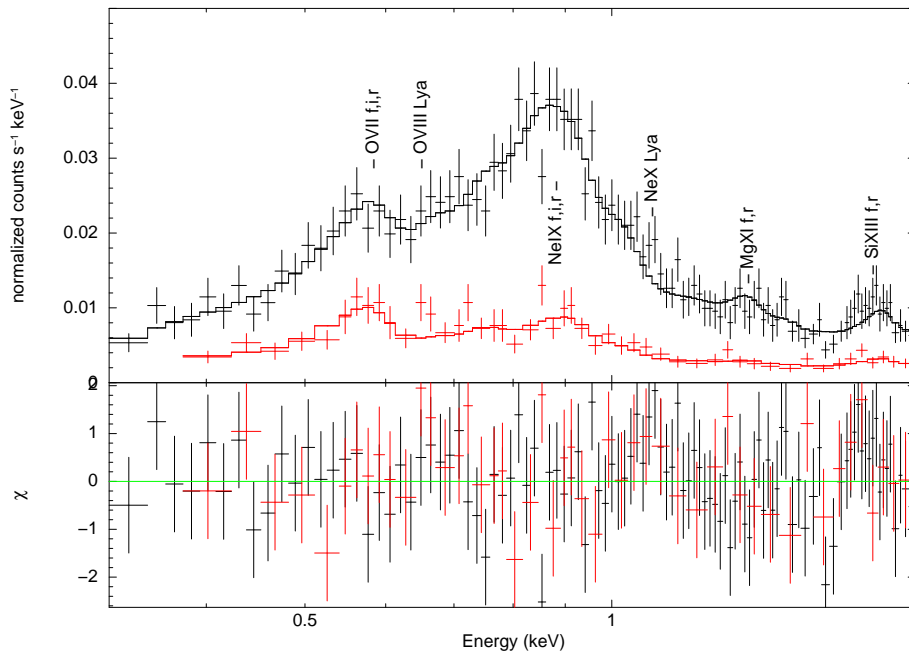


Fig. 5.— Spectral fit of the X-ray emission in hot spot (black) and surrounding regions (red). Likely identifications of the blended emission lines are labeled, based on the HETG line list in Ogle et al. (2000). See text and Table 1 for model details.

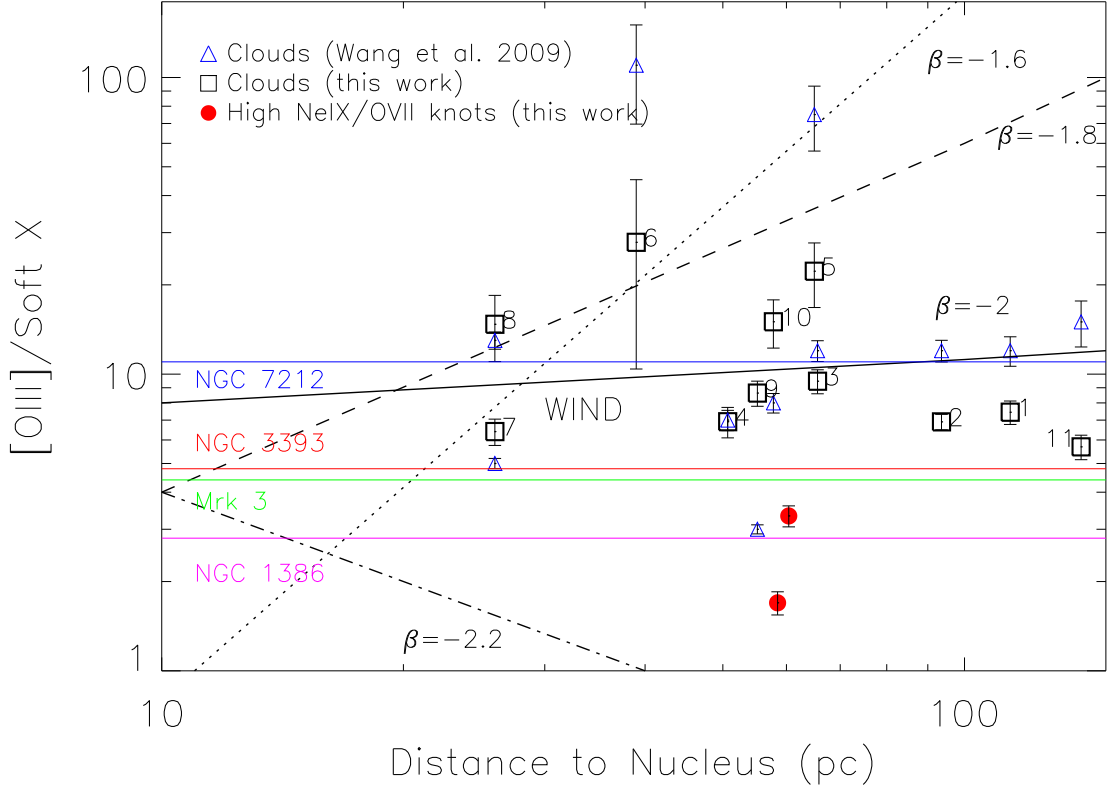


Fig. 6.— The [OIII] to soft X-ray ratio as a function of the cloud’s distance to the nucleus. The triangles are the measurements in Wang et al. (2009), and the squares are from this work. The filled (red) circles represent the two high NeIX/OVII ratio regions (Figure 4). The blue, red, green, and magenta lines indicate the [OIII]/X-ray ratios for NGC 7212, NGC 3393, Mrk 3, and NGC 1386 (Bianchi et al. 2006), respectively. The dotted, dashed, solid, and dot-dashed lines are the Cloudy model predicted values from Bianchi et al. (2006) for different radial density profiles: $n_e \propto r^\beta$ where $\beta = -1.6, -1.8, -2,$ and $-2.2,$ respectively.

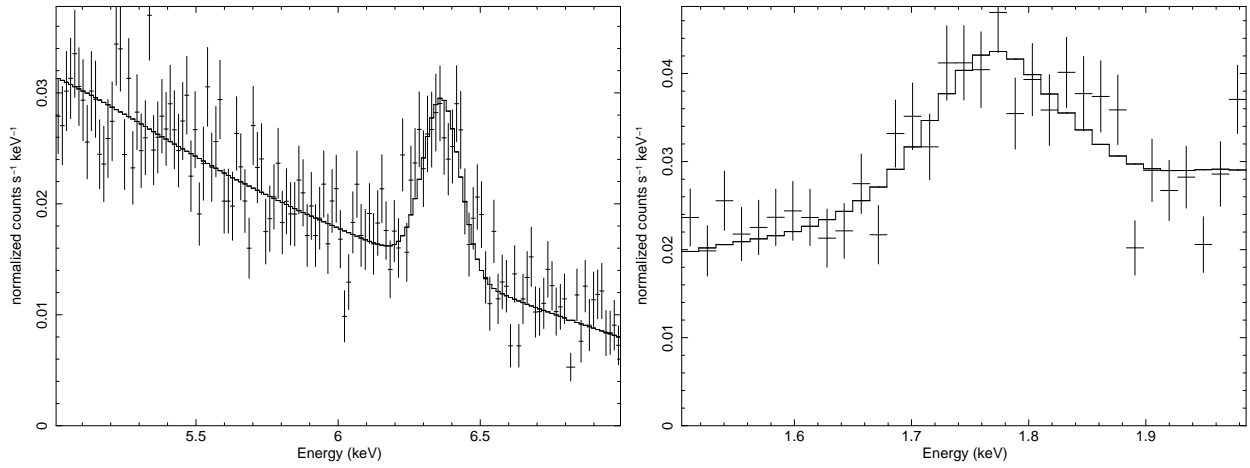


Fig. 7.— (a) The spectrum of the extended emission showing presence of Fe K α line. (b) Same spectrum but showing the Si K α line part. The underlying solid line is the NGC 4151 nuclear spectrum (modeled with a power law plus a gaussian), scaled to 6% and 3% of the nuclear flux, respectively.

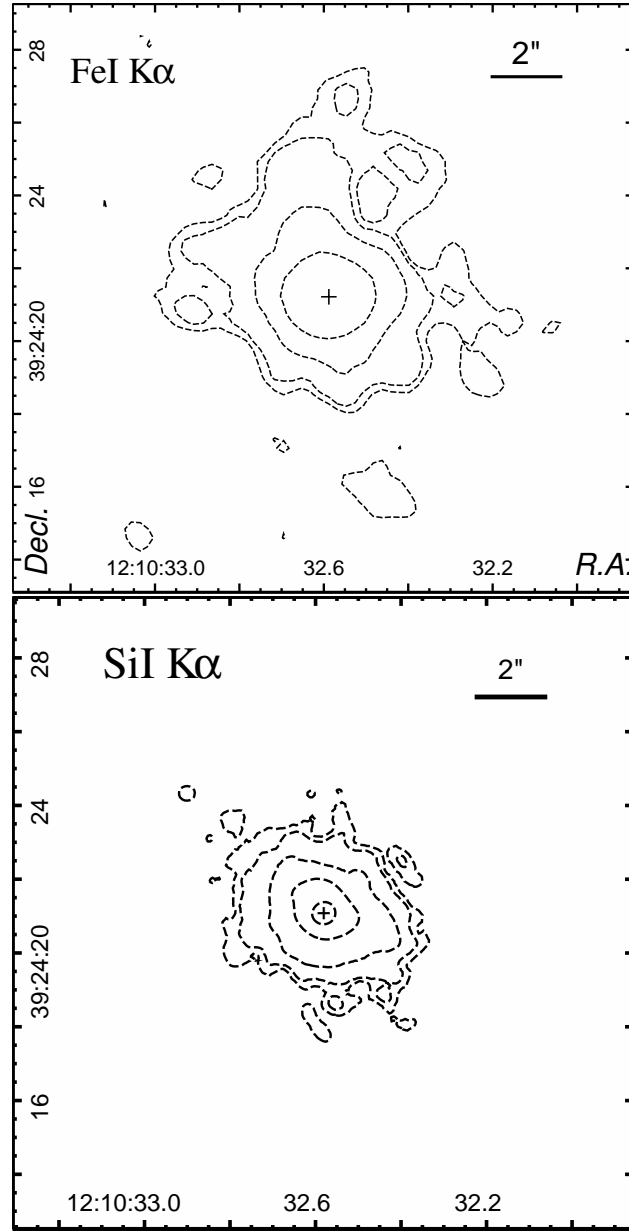


Fig. 8.— (a) The contour map of continuum-subtracted Fe $K\alpha$ line emission of the central $15'' \times 15''$ region in NGC 4151. (b) The contour map of SiI $K\alpha$ line emission of the same region, extracted between 1.7 keV and 1.8 keV. The cross marks position of the nucleus. The contour levels are of logarithmic scale, between 3×10^{-10} to 4×10^{-8} photons $\text{cm}^{-2} \text{s}^{-1}$.

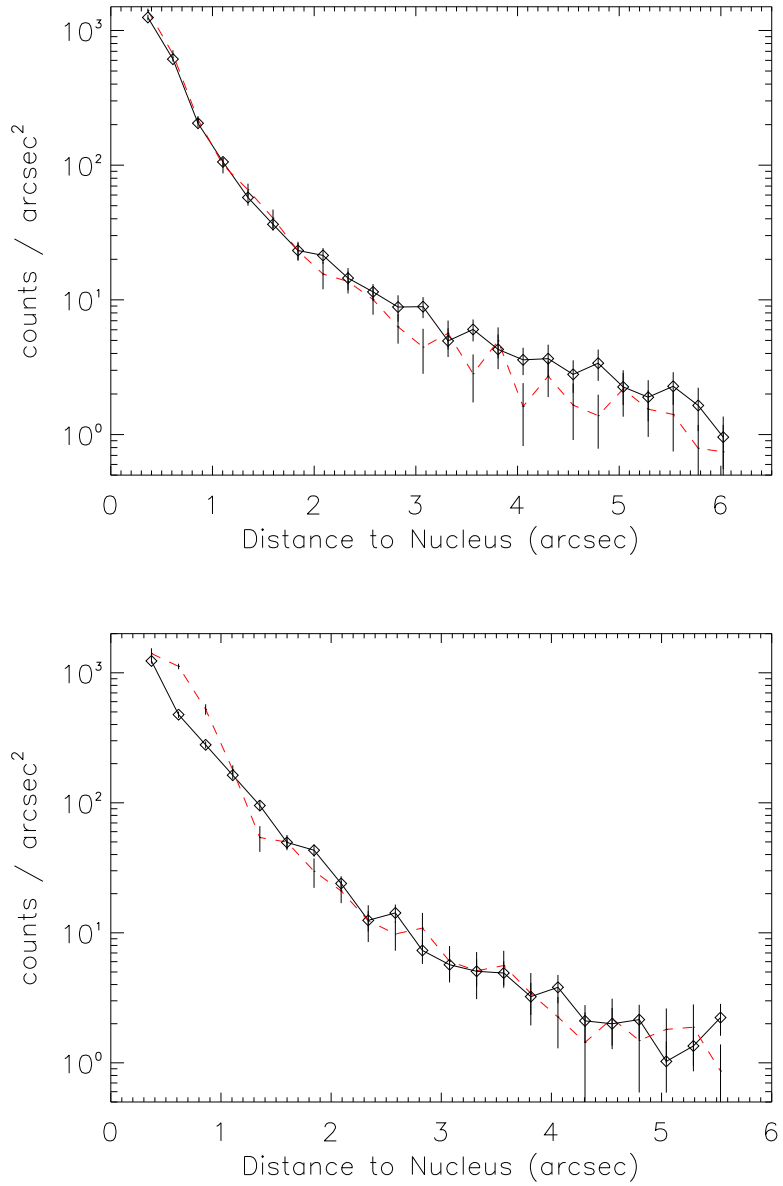


Fig. 9.— (a) Comparison between the radial profile of simulated PSF in the 6.2–6.5 keV band (red dashed line) and the observed narrow-band Fe $K\alpha$ line emission (black solid line). (b) The same comparison but for the 1.7–1.8 keV Si $K\alpha$ line emission band.

Table 1. Spectral Fits to the NeIX/OVII Enhancements and Surrounding Region

Region	Counts [0.3–2 keV]	$\log U_1$	$\log N_{H,1}$ [cm ⁻²]	<i>Norm1</i>	$\log U_2$	$\log N_{H,2}$ [cm ⁻²]	<i>Norm2</i>	<i>kT</i> [keV]	<i>Norm3</i>	Nuclear PSF ^a	$F_{0.3-2keV}$ ^a [erg s ⁻¹ cm ⁻² arcsec ⁻²]
High-ratio	4585	-0.01 ± 0.03	20.5	8.0 × 10 ⁻¹⁶	1.9 ± 0.2	22.5	1.5 × 10 ⁻¹⁸	0.58 ± 0.05	1.8 × 10 ⁻⁵	1455 ± 35	8.9 × 10 ⁻¹⁴
Low-ratio	1317	-0.01 ± 0.03	20.5	8.2 × 10 ⁻¹⁶	1.9 ± 0.2	22.5	6.3 × 10 ⁻¹⁹	0.58 ± 0.05	4.5 × 10 ⁻⁶	530 ± 23	6.8 × 10 ⁻¹⁴

^aThe absorption column N_H is fixed at 2×10^{20} cm⁻² (Murphy et al. 1996), the Galactic column towards NGC 4151; χ^2 / d.o.f.= 146/142 for the best fit presented here.

^bExpected counts from simulation of PSF scattered nuclear emission in the 0.3–2 keV band.

^cSoft X-ray surface brightness of the extended emission after nuclear emission removed.

Table 2. Measured X-ray and [OIII] Fluxes

Cloud label	Distance to Nuc. (")	Distance to Nuc. (pc)	[OIII] flux (10^{-13} erg s $^{-1}$ cm $^{-2}$)	Net Counts (0.3-2 keV)	0.5-2 keV Flux ^a (10^{-14} erg s $^{-1}$ cm $^{-2}$)	[OIII]/soft X (ACIS)	[OIII]/soft X (HRC)
1	1.76	114	1.1	369±24	1.5	7.4	12
2	1.44	93.6	1.9	688±29	2.7	6.9	12
3	1.01	65.6	2.2	581±38	2.3	9.4	12
4	0.78	50.7	1.3	470±39	1.9	6.9	7
5	1.0	65.0	1.5	168±29	0.7	22.2	75
6	0.6	39.	1.1	99±44	0.4	27.8	110
7	0.4	26.	3.4	1320±96	5.3	6.4	5
8	0.4	26.	3.3	560±100	2.2	14.7	13
9	0.85	55.2	2.4	694±47	2.8	8.6	3
10	0.89	57.8	1.6	266±35	1.1	15.0	8
11	2.15	139.7	0.6	264±17	1.1	5.7	15
C2 ^b	0.9	58.5	0.8	1180±44	4.7	1.7	2
C5 ^b	0.93	60.4	1.4	1052±43	4.2	3.3	3

^aAn average conversion factor 7.2×10^{-12} erg s $^{-1}$ cm $^{-2}$ (counts s $^{-1}$) $^{-1}$ is derived from spectral models in Table 1 to estimate flux from net count rate.

^bC2 and C5 are the radio knots in Mundell et al. (1995), corresponding to the locations of high NeIX/OVII ratio hot spots to the east and west of the nucleus, respectively.